# A programmable dark-field detector for imaging two-dimensional materials in the scanning electron microscope

Benjamin W. Caplins[a], Jason D. Holm[a], and Robert R. Keller[a]

[a]National Institute of Standards and Technology, 325 Broadway, Boulder, CO, USA 80305

## ABSTRACT

Unit cell orientation information is encoded in electron diffraction patterns of crystalline materials. Traditional transmission electron detectors implemented in the scanning electron microscope are highly symmetric and are insensitive to in-plane unit cell orientation information. Herein we detail the implementation of a transmission electron detector that utilizes a digital micromirror array to select anisotropic portions of a diffraction pattern for imaging purposes. We demonstrate that this detector can be used to map the in-plane orientation of grains in two-dimensional materials. The described detector has the potential to replace and/or supplement conventional transmission electron detectors.

**Keywords:** digital micromirror device (DMD), scanning electron microscope (SEM), scanning transmission electron microscopy (STEM), transmission electron detector

## 1. INTRODUCTION

The scanning electron microscope (SEM) is widely used for imaging the surfaces of materials over six orders of magnitude in scale ($10^{-3}$ m to $10^{-9}$ m).[1] In an SEM, a focused electron beam (*ca.* 1 nm diameter on modern field emission SEMs) is scanned across the surface of a bulk sample in a raster pattern. At each point on the sample, the electron beam interacts with the sample and generates a signal that is measured to create an image. By far, the most common signal measured to generate an image is known as the secondary electron (SE) signal, comprised of low-energy inelastic electrons, emitted in the backscatter direction. Generally, these electrons are collected over a large solid angle with an Everhart-Thornley detector[2] and are relatively insensitive to the sample crystallography. When applied to 2D materials, SE images are generally used for their topographic,[1] work function,[3] or material-dependent SE-yield[4] contrast mechanisms.

For nanomaterials in an SEM, where the electron mean free path at 30 keV can be comparable to the material thickness, most of the incident electrons undergo small-angle scattering events and transmit through the sample (Figure 1a). This transmitted electron scattering distribution forms a diffraction pattern in the far-field, and portions of it can be detected to create real-space images. Experimental diffraction patterns of amorphous and crystalline materials are shown in Figure 1b. In the SEM, transmission electron detectors are usually axially symmetric and integrate circular or annular regions of the diffraction pattern (e.g. Figure 1a). When the central disk of the diffraction pattern is spatially integrated, the corresponding image is called a 'bright field' (BF) image. Conversely, if some portion of the area outside the central disc is spatially integrated, the corresponding image is called a 'dark-field' (DF) image. A common type of DF image is the annular dark-field (ADF) image. While these imaging modes enable mass-thickness measurements,[1] they generally do not contain interpretable crystallographic information in an SEM for 2D materials.

To obtain image contrast based on crystallographic orientation of 2D materials, a non-axially symmetric portion of the diffraction pattern needs to be integrated. As an example, we use the six-fold symmetric diffraction



Further author information: (Send correspondence to B.W.C.)
B.W.C.: E-mail: benjamin.caplins@nist.gov
J.D.H.: E-mail: jason.holm@nist.gov
R.R.K.: E-mail: bob.keller@nist.gov

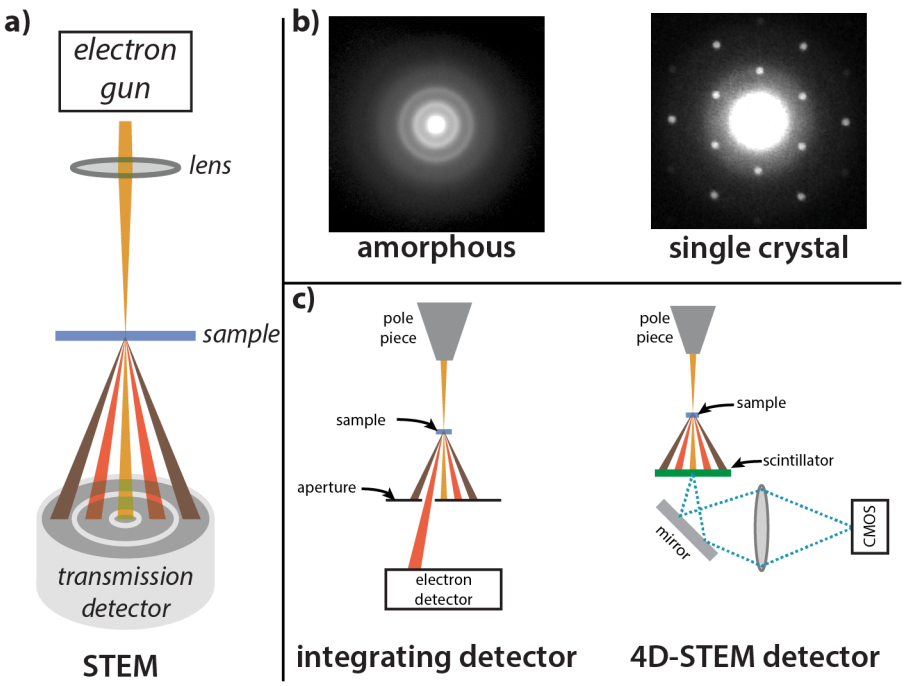


Figure 1. (a) Schematic of a scanning transmission electron microscope. An electron gun emits electrons which are focused onto a thin, electron-transparent sample. The transmitted electrons then strike an electron detector. (b) Example electron scattering distributions (30 keV) incident on a transmission detector. The left image shows an axially symmetric diffraction pattern from an amorphous material, while the right image shows an anisotropic diffraction pattern from a crystalline material. The diffraction pattern on the right is from a single crystal region of monolayer graphene. (c) Two types of detectors capable of discerning anisotropy in crystalline diffraction patterns. A physical mask may be used to isolate a subset of the diffracted electrons, which are then summed on an integrating detector. Alternatively, the full diffraction pattern may be imaged and saved for each beam position resulting in a four dimensional dataset, $I(x, y, k_x, k_y)$ (i.e., 4D-STEM).

pattern of graphene in Figure 1b. To generate orientation contrast, the imaging mask must collect the diffracted electrons from a specific graphene orientation, while rejecting the diffracted electrons from other, rotated domains.

There are currently two methods to accomplish this goal. In the first method, a physical mask is placed over a high-bandwidth integrating detector to select a subset of the scattered electrons (Figure 1c).[5] Alternatively, the active area of the detector is constructed to have a defined shape. This method has the benefit of being simple to implement using high-bandwidth integrating electron detectors that can collect megapixel images in just a few seconds. However, these integrating detectors cannot reconstruct the full diffraction pattern, meaning that it is not always known what scattering conditions are being selected. An additional challenge is that it is difficult to manipulate the orientation of a physical mask/detector inside a vacuum chamber.

In the second method referred to as 4D-STEM, the diffraction pattern is collected for each beam position resulting in a four dimensional dataset, $I(x, y, k_x, k_y)$. Either a pixelated direct electron detector[6] (not commercially available for SEMs at this time) or a scintillator/camera combination[7] (Figure 1c) can be used to collect this data. With the 4D dataset in hand, the in-plane crystallographic orientation can be deduced from the diffraction patterns. Unfortunately, the 4D-STEM method suffers from the relatively slow readout rate of cameras ($\approx 10^3$ frames per second) resulting in $\approx 10^3$ seconds per scan. Furthermore, the large datasets are only sparsely populated with information and are, at present, unwieldy to transfer and analyze.

Herein, a new transmission detector called the programmable scanning transmission electron microscope (p-STEM) detector is described.[8,9] This detector utilizes a digital micromirror device (DMD) to give direct access

to the full electron diffraction pattern, with the additional capability to rapidly create targeted DF images, that can emphasize the crystallographic orientation of the sample. In many ways, this detector is a modern realization of a detector suggested by Cowley and Spence in 1979, which used tiny mirrors on actuators in place of a DMD.[10]

As a proof of principle, we use the p-STEM detector to map the in-plane orientation of a graphene sample and generate diffraction contrast from multilayer graphene. To date, orientation mapping of graphene has not been demonstrated with any other method in an SEM; this represents one of the most difficult samples to characterize due to carbon's low scattering cross section.[11] To generate grain orientation maps of graphene, one could resort to performing conventional DF transmission electron microscopy (TEM).[12,13] Due to DMD technology, however, we can perform this characterization in widely available and accessible SEMs.

## 2. DETECTOR CONSTRUCTION

A preliminary description of the detector's basic optical design and construction was given previously,[8] and a followup manuscript described the incorporation of the detector into an SEM and showed proof-of-principle data on several material samples.[9] Here we provide a brief overview of the detector with an emphasis on describing the light collection efficiency as it directly influences the overall detector quantum efficiency (DQE) of the p-STEM detector.*

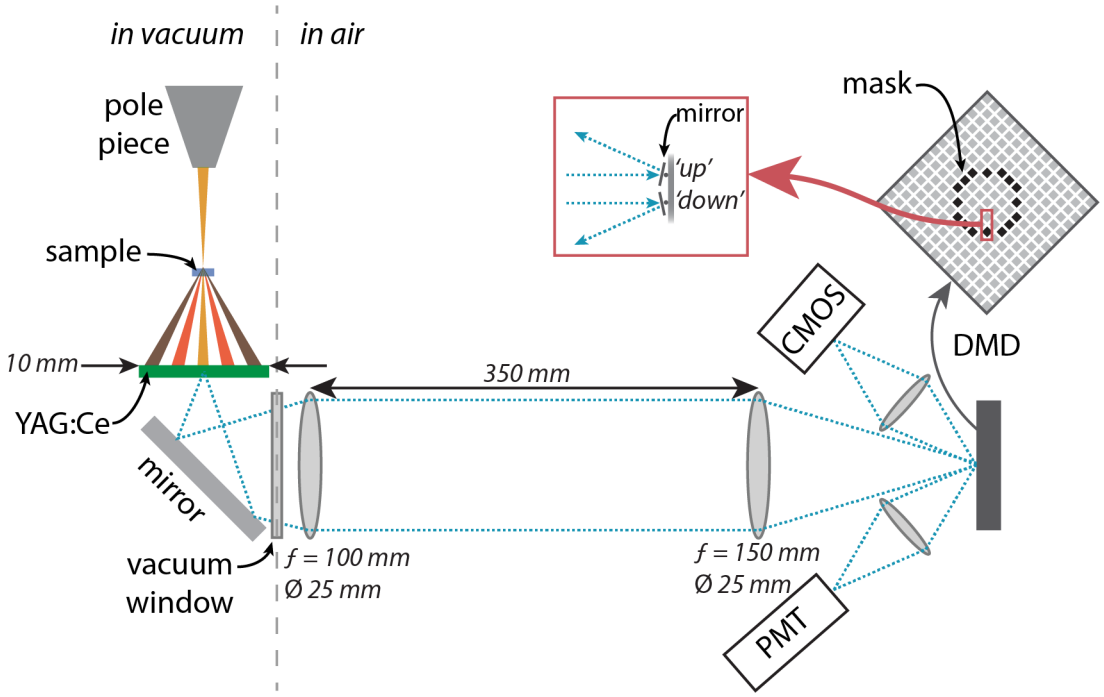


Figure 2. Schematic of the programmable scanning transmission electron microscopy (p-STEM) detector. A focused electron beam is scanned across a thin, electron transparent sample. The transmitted electrons strike a YAG:Ce crystal (Crytur, $t = 100\,\mu m$ , $\phi$ 12.7 mm, 50 nm Al top-coat, AR bottom-coat) which emits photons. These photons are imaged out of the vacuum chamber through a window (Eksma Optics, 220-1203M+ARB625) and onto a DMD (Vialux, V-7000) with an achromat pair (Thorlabs, AC254-100-A, AC254-150-A). The upper arm images the DMD surface to a CMOS camera (IDS, UI-3252LE) positioned at the Scheimpflug image plane. The lower arm images (Thorlabs, MAP052550-A) the DMD surface to a PMT (Hamamatsu, H10721-210) which is amplified (Stanford Research, SRS570) before being sent into the auxiliary detector input of an SEM (Zeiss, GeminiSEM 300). The SEM, CMOS camera, and DMD are controlled via software developed in-house.

*Commercial instruments, equipment, or materials are identified only in order to adequately specify certain procedures. In no case does such an identification imply recommendation or endorsement by NIST, nor does it imply that the products identified are the best available for the purpose.

## 2.1 Detector Hardware

The electron detector is constructed as shown in Figure 2 and can be separated into three parts: photon generation, photon transport, and photon detection. Photons are generated when the transmitted electrons strike a YAG:Ce scintillator crystal. Monte Carlo simulations (not shown) can provide insight into the photon generation process.[14] For example, simulations have shown that at a 30 keV beam energy, approximately 15 % of incident electron kinetic energy is lost due to electrons backscattered out of the scintillator. The remaining energy is deposited on the order of 1 $\mu$m deep into the scintillator material, far from the aluminum coating which might quench the excited $Ce^{3+}$ ions. The conversion efficiency given for the YAG:Ce is 30 photons per keV ($\lambda = 547$ nm) which gives a yield of 765 photons per electron which we assume are isotropically emitted.

While the photon generation step has a large intrinsic gain, the photon transport from the scintillator to the detector has a significant loss. The dominant loss is due to the small solid angle collected by the imaging optics. Only approximately 1 in 1000 photons is collected, which effectively cancels the gain of the electron generation step. An electron transparent, optically reflective coating (50 nm of aluminum) on the top surface of the YAG:Ce crystal enhances the photon collection efficiency, while the reflective losses in the optical system slightly degrade the photon collection efficiency. In the final step, the photons are detected by a photomultiplier tube, which has a low quantum efficiency (QE) at visible wavelengths. These steps and their relative gain/loss coefficients for the detector configuration used here are given in Table 1.

Table 1. Steps in the photon generation, transport, and detection chain with calculated gain and loss coefficients. The total efficiency is the product of all the coefficients.

| **step** | **coefficient** | **notes** |
|---|---|---|
| deposition of energy into the scintillator | 0.85 | Loss due to electron backscattering estimated from Monte Carlo simulation.[14] |
| energy to photon conversion | 765 | Assumes 30 photons ($\lambda = 547$ nm) generated per 1 keV energy deposited with a 30 keV electron beam. Value from manufacturer.[15] |
| increase in effective source intensity due to reflective coating | 1.9 | Assumes a 90 % reflectance from 50 nm Al.[16] |
| fraction of solid angle collected | $9.7 \times 10^{-4}$ | Assumes the $\phi$ 22.9 mm clear aperture of a $f = 100$ mm lens is the limiting aperture. Includes the change in refractive index going from YAG:Ce ($n = 1.82$) to air ($n = 1$). |
| reflective losses | 0.9 | Assumes 99 % transmission (reflectivity) from the various glass (mirror) surfaces. Lenses and vacuum window have antireflective coatings. |
| loss from DMD | 0.65 | Includes DMD fill factor, reflectivity, window transmission, and diffraction efficiency as quoted by the DMD manufacturer.[17] |
| photomultiplier quantum efficiency (QE) | 0.12 | As quoted from PMT manufacturer.[18] |

Combining the gain/loss coefficients, we calculate that for every electron that strikes the scintillator there is a 8.4 % chance that it is detected, which gives a DQE of 0.078 assuming the detector has no noise sources other than counting statistics.[19] Table 1 suggests there are two main routes to improve detector efficiency – the detector QE and the photon efficiency. First, the QE of the detector is 0.12, which leaves significant room for improvement. For example, a GaAsP PMT achieves *ca.* 40 % QE at 550 nm,[20] though for some dark-field imaging applications the DQE could be degraded by the relatively high dark count rate of such detectors. Second, and most important, the collection efficiency of the optics is poor – on the order of 0.1 %. To improve this, larger numerical aperture lenses could be used, albeit at the expense of either increased aberration/distortion and/or reduced field of view.

Experimentally we estimated the probability of electron detection as 0.035 via a photon counting approach. Briefly, at a very low electron beam current the beam current is measured with a Faraday cup. Under effectively identical conditions, the photon count rate was also measured. For low DQEs, the ratio of the photon count rate to electron beam current in electrons per second yields the average number of photons detected per electron incident on the scintillator. The dominant source of error arises from the the difficulty in detecting a photon event in the PMT signal. By adjusting the photon detection criteria within a reasonable range, we estimate an uncertainty of at least to 20 % on the measured probability of electron detection.

The values in Table 1 result in an average photon yield approximately twice that of the photon counting measurement, though this is not unexpected. The calculation assumes the literature/manufacturer values are accurate for the scintillator conversion efficiency and PMT QE, but theses values are known to vary from batch to batch, and the conditions under which they were determined are not specified. Additionally, the calculation assumes the optical system is perfectly aligned, which is likely not the case due to the difficulty of aligning an optical system with the physical constraints imposed by the vacuum chamber. In any case, the calculated and measured detection probabilities are in qualitative agreement, suggesting that the limitations of the optical assembly are understood. We note that we do not characterize the CMOS camera arm of the optical assembly, because the integration times for diffraction patterns are generally many orders of magnitude longer than the dwell times used for SEM image acquisition.

Finally, it is worth placing the DQE measurements/calculations in the context of an actual DF imaging experiment in an SEM. The beam current on a field emission SEM is on the order of 300 pA which corresponds to $2 \times 10^9$ electrons per second. For monolayer graphene, a kinematic scattering calculation predicts $\approx 0.2$ % of the beam will scatter into the 2nd order diffraction spots. For a DF image based on the 2nd order diffraction spots, the scattering efficiency, and the DQE, result in an electron detection rate of *ca.* $2.9 \times 10^5$ electrons per second. This count-rate is notable for two reasons. First, the PMT selected for the p-STEM detector has a dark count rate several orders of magnitude below this expected signal, and thus should not add additional noise. Second, because of the high contrast intrinsic to DF images, a 1 megapixel DF image should be able to be acquired on the order of minutes with a signal to noise in excess of the Rose criterion. In this manuscript, integration times for single DF images were $\leq 120$ s, in reasonable agreement with this estimate.

### 2.2 Detector Software

To utilize the p-STEM detector in an experiment, software was developed to control the SEM, the DMD, and the two optical detectors (PMT and CMOS camera) simultaneously. Two main modes were developed. In 'diffraction mode' the user can load an SEM micrograph into a graphical user interface (GUI) and select several regions of the sample from which to collect diffraction patterns. In this mode, the program tilts all the micromirrors towards the CMOS camera, positions the electron beam at the locations on the sample specified by the user, and then collects and saves the diffraction patterns. These diffraction patterns are then corrected for optical imaging distortions using an affine transform and presented to the user.

In 'imaging mode', the user loads in diffraction patterns from regions on their sample. Then using the GUI, the user can create various digital masks to apply to the DMD which will serve as a digital 'objective aperture' to collect bright and dark field images of the sample. The types of masks that are currently included in the GUI are circular, annular, two dimensional lattices, user selected spots, and combinations thereof. More complex masks can be generated via external scripts. Once the user has specified a diffraction mask, the mask is mapped to the DMD image plane and applied to the DMD. The user can then collect images with the SEM software using the output of the PMT as the signal source. Further details on the method of mapping the diffraction images and masks to different image planes is given in a previous manuscript.[9]

## 3. APPLICATIONS OF THE DETECTOR TO GRAPHENE

### 3.1 Orientation Contrast in Monolayer Graphene

As a proof-of-principle we use graphene samples on a lacey carbon support (Ted Pella, 21710) to show orientation-based contrast with the p-STEM detector. These films consist of continuous, mostly flat monolayer graphene across the TEM grid with small patches of bilayers. Folds and wrinkles of the graphene are also present. Coating

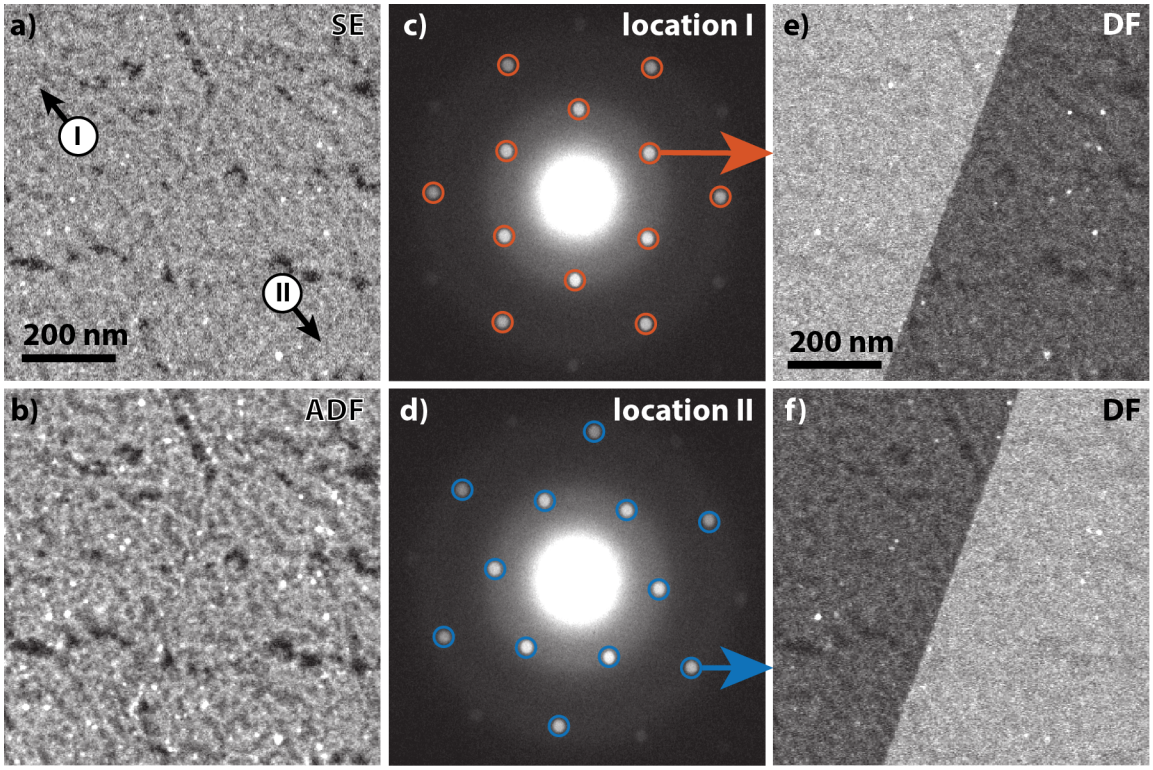


Figure 3. This figure shows how the p-STEM detector can yield orientation contrast from graphene samples that is totally absent from conventional SEM imaging modes. All real-space images are from the same field-of-view. (a) A SE image of a monolayer graphene sample. (b) An ADF image. Neither of these 'conventional' SEM imaging modes show any measurable orientation contrast from the graphene – they only show debris on the graphene surface. (c,d) Diffraction patterns from the two locations specified in (a). The two diffraction patterns are rotated 23° with respect to one another. (e,f) DF images collected by masking the diffraction patterns as shown in (c,d).

the graphene films is a mixture of amorphous (polymer leftover from a transfer step) and crystalline (assumed to be leftover salts from the etching and lift-off process) materials.

Figure 3 shows conventional SEM imaging modes in addition to diffraction contrast images made possible by the p-STEM detector. Figure 3a is an SE image taken with a conventional Everhart-Thornley detector, and Figure 3b is an ADF image taken with an annulus that is set to accept the signal from (transmitted) electrons diffracted by the graphene lattice. Both images show similar features, though the ADF image has greater signal to noise. The small dark patches are likely clean graphene, while the grey texture that coats the surface is assigned as adsorbed organic – likely polymer residue.[21] The small bright spots ($\approx$ 10 nm) are crystalline debris.

Figure 3c-d show diffraction patterns collected in 'diffraction mode' at locations I and II as specified in Figure 3a. The diffraction patterns show two main features. First, they show the first three diffraction orders from graphene as spots (the 3rd order is extremely weak as expected). The relative intensity of the 1st and 2nd order diffraction spots was measured to be close to 1 and indicates that the graphene is monolayer thickness.[22] The two diffraction patterns show a 23° relative orientation. Second, low intensity diffuse rings are visible near the 1st and 2nd order diffraction spots. These rings are due to the amorphous debris coating the sample. Prolonged exposure to the electron beam will increase these diffuse rings via electron-beam-induced sample contamination.

Figure 3e-f show DF images collected by creating two different DF masks that collect the diffraction spots of each diffraction pattern in Figure 3c-d. In these images, there is a clear contrast between the left and right sides of the field of view separated by a distinct interface. This interface is a grain boundary, and the spatial resolution is limited only by that of the SEM image. We note that this interface is not visible in conventional

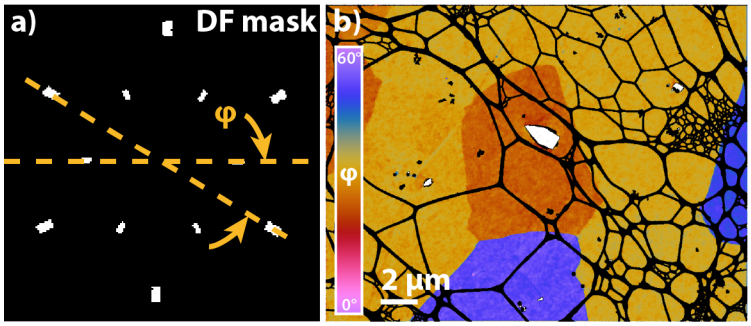


Figure 4. This figure shows how the p-STEM detector can perform orientation mapping of graphene. (a) A DF mask is designed to overlap with the 1st and 2nd order graphene diffraction spots over a finite angular range of the in-plane orientation angle, $\phi$. A series of 30 such masks are generated for $\phi \in \{0°, 2°, 4°...58°\}$ and a DF image is collected for each mask. From this stack of images, an orientation map can be constructed and is displayed in (b). Here the lacey carbon is colored black, and holes in the graphene sheet are colored white. Several grains with different orientation are obvious in the field of view.

SEM imaging modes (BF, ADF, SE) regardless of the image processing steps taken. The data show that the p-STEM detector is capable of obtaining image contrast not available with conventional SEM imaging modes.

Once this diffraction contrast is observed, it is relatively straightforward to develop an automated method for mapping the orientation of graphene domains. Here, a series of digital masks is generated that has the symmetry of the graphene diffraction pattern, but with each mask having a different in-plane orientation parameterized by $\phi$ (Figure 4a). By generating a series of these masks that span the angular range $\phi \in [0°, 60°]$ and collecting a DF image for each mask, we can determine the orientation of the graphene lattice at each pixel. Figure 4b shows an orientation map with several grains of graphene visible. To obtain high quality orientation maps, we performed rigid image registration to account for sample drift.[23] Additionally, the data in Figure 4b was filtered with a total variational denoising algorithm on each DF image prior to computing the orientation. Total variation denosing significantly reduces the noise in piecewise constant images without smoothing the edges (i.e. grain boundaries).[24] In the present work, we used a first circular moment analysis of the image stack to obtain the graphene orientation.[25] More advanced peak finding or pattern matching methods[26] would likely be more accurate at an increased computational cost.

### 3.2 Orientation Contrast in Bilayer Graphene

In addition to mapping the orientation contrast in monolayer graphene films, this detector can be used to map the orientation in bilayer films. Figure 5a shows a SE image of a graphene film. Diffraction patterns were collected at location I and II as indicated and are shown in Figure 5b-c respectively. Location II shows only a single orientation of graphene, while location I shows a two orientations of graphene. Three DF images were collected corresponding to the masks shown. The DF image corresponding to the dotted blue mask in Figure 5b represents a background image due to electrons scattered from the surface debris and lacey carbon. Figure 5e-f correspond to the two DF masks that each collected the electrons scattered from a particular graphene lattice orientation. The data show that there is an annular shaped island of graphene on top of a continuous graphene sheet.

### 3.3 Moire Fringe Contrast in Multilayer Graphene

Multiple layers of graphene with nearly the same orientation will give rise to moire fringes/patterns in DF images. If visible, these periodic signals give insight into the local stacking of graphene multilayers. Figure 6a shows a diffraction pattern collected from a multilayer region of graphene. Three DF images were collected (Figure 6b-d) using the three diffraction spots specified. In all three DF images, moire fringes are readily visible signifying strain and/or misorientation between the layers.[27]

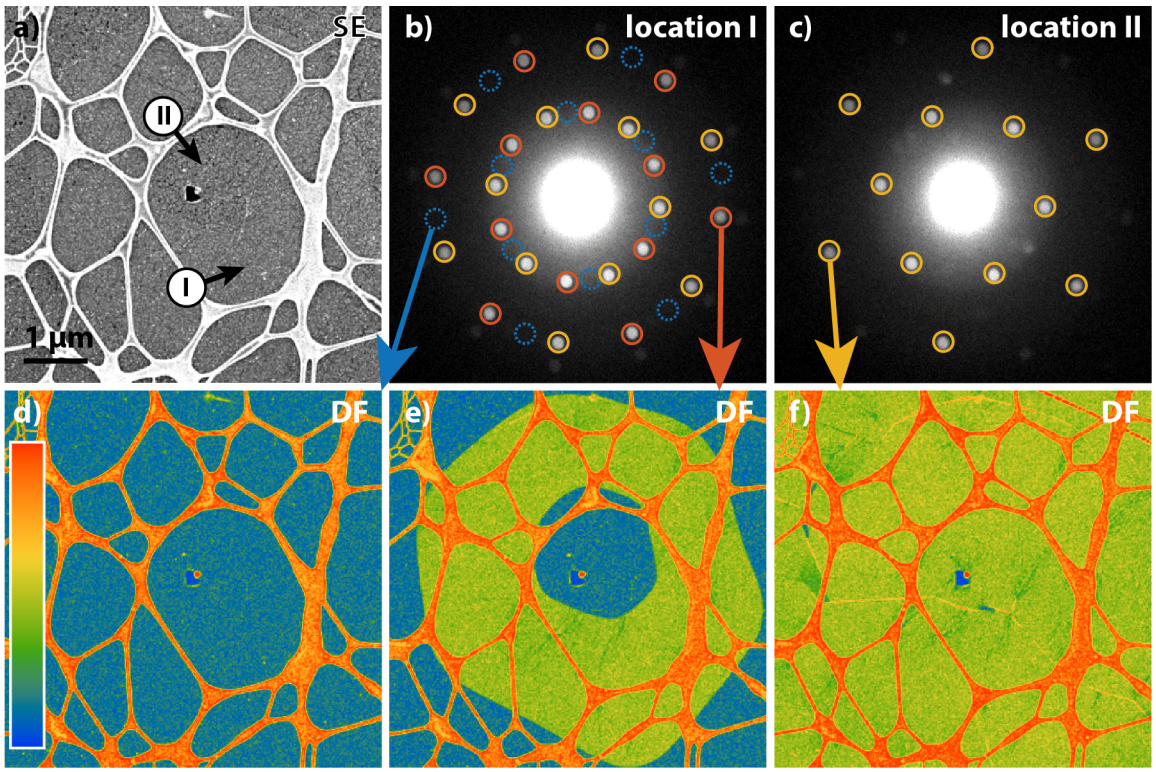


Figure 5. This figure shows how the p-STEM detector can characterize the orientation of graphene bilayers. (a) A SE image of a region of a graphene film supported on lacey carbon. (b,c) Diffraction patterns collected at the two locations specified in (a). Location I shows two graphene diffraction patterns with a relative orientation of 30°, while location II only shows one of the two graphene orientations. (d,e,f) DF images collected by masking the diffraction patterns as shown in (b,c). Since the DF mask used to collect (d) is not coincident with a graphene lattice, it serves as a background image due to scattering from surface debris and the lacey carbon. Here the lacey carbon is colored red, the surface debris is colored blue. In (e,f) graphene shows up as green due to the fact the the mask is capturing the electrons scattered by the graphene lattice. These images show that while the conventional SE image is not sensitive to the layer number and orientation of the graphene lattice, the DF images can easily discern the presence of a rotated bilayer island on a contiguous graphene monolayer support.

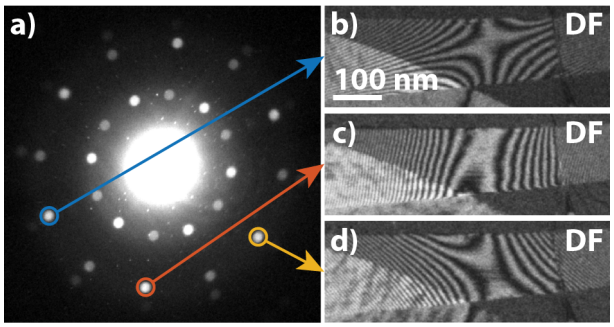


Figure 6. This figure highlights that the DF imaging afforded by the p-STEM is sensitive to lattice strain. (a) A diffraction pattern is collected from the field of view in (b,c,d). (b,c,d) DF images collected by masking a single 2nd order graphene diffraction spot as specified in (a). Moire fringes are readily visible and contain information on the local stacking of graphene multilayers.

## 4. CONCLUSIONS

Traditional imaging modes in an SEM have limited sensitivity to the crystallographic orientation of 2D materials. Herein, crystallographic contrast was not observed on monolayer graphene when using an Everhart Thornley SE detector or a BF or ADF transmission electron detector. The basic problem is that orientational contrast requires a non-axially symmetric detector capable of differentiating in-plane rotations. One method to construct a detector sensitive to in-plane orientation uses a DMD in an image plane conjugate to the diffraction pattern to serve as a programmable DF mask. By incorporating DMD technology into the p-STEM detector, we are able to switch between 'imaging' and 'diffraction' modes without any macroscopic moving parts. This allows the user to perform all DF masking operations digitally. We demonstrate that the p-STEM detector has the potential to characterize grain orientation in 2D materials. We believe that DMD technology will enable the SEM to be used to investigate phenomena that previously required the use of a TEM.

## ACKNOWLEDGMENTS

We thank Ryan White (NIST) and Ann Chiaramonti Debay (NIST) for helpful microscopy related discussions, and Callie Higgins (NIST) for discussions related to optics. This work was performed while B.W.C. held a National Research Council Postdoctoral Associateship. The authors also thank the NIST Small Business Innovation Research Program for supporting RadiaBeam Technologies' detector development under Contract SB1341-14-CN-0026.

## REFERENCES

[1] Goldstein, J. I., Newbury, D. E., Echlin, P., Joy, D. C., Lyman, C. E., Lifshin, E., Sawyer, L., and Michael, J. R., [*Scanning Electron Microscopy and X-ray Microanalysis*], Springer US, Boston, MA (2003).

[2] Everhart, T. E. and Thornley, R. F. M., "Wide-band detector for micro-microampere low-energy electron currents," *Journal of Scientific Instruments* **37**, 246–248 (jul 1960).

[3] Zhou, Y., Fox, D. S., Maguire, P., O'Connell, R., Masters, R., Rodenburg, C., Wu, H., Dapor, M., Chen, Y., and Zhang, H., "Quantitative secondary electron imaging for work function extraction at atomic level and layer identification of graphene," *Scientific Reports* **6**, 21045 (aug 2016).

[4] Yoo, Y., Degregorio, Z. P., and Johns, J. E., "Seed Crystal Homogeneity Controls Lateral and Vertical Heteroepitaxy of Monolayer MoS2and WS2," *Journal of the American Chemical Society* **137**(45), 14281–14287 (2015).

[5] Holm, J. and Keller, R. R., "Angularly-selective transmission imaging in a scanning electron microscope," *Ultramicroscopy* **167**, 43–56 (aug 2016).

[6] Faruqi, A. and McMullan, G., "Direct imaging detectors for electron microscopy," *Nuclear Instruments and Methods in Physics Research Section A: Accelerators, Spectrometers, Detectors and Associated Equipment* **878**, 180–190 (jan 2018).

[7] Fundenberger, J. J., Bouzy, E., Goran, D., Guyon, J., Yuan, H., and Morawiec, A., "Orientation mapping by transmission-SEM with an on-axis detector," *Ultramicroscopy* **161**, 17–22 (2016).

[8] Jacobson, B. T., Gavryushkin, D., Harrison, M., and Woods, K., "Angularly sensitive detector for transmission Kikuchi diffraction in a scanning electron microscope," *Proceedings of SPIE of SPIE* **9376**(310), 93760K (2015).

[9] Caplins, B. W., Holm, J. D., and Keller, R. R., "Transmission imaging with a programmable detector in a scanning electron microscope," *Ultramicroscopy* **196**, 40–48 (jan 2019).

[10] Cowley, J. and Spence, J., "Innovative imaging and microdiffraction in stem," *Ultramicroscopy* **3**, 433–438 (jan 1978).

[11] Reimer, L., [*Scanning Electron Microscopy*], vol. 45 of *Springer Series in Optical Sciences*, Springer Berlin Heidelberg, Berlin, Heidelberg (1998).

[12] Kim, K., Lee, Z., Regan, W., Kisielowski, C., Crommie, M. F., and Zettl, A., "Grain Boundary Mapping in Polycrystalline Graphene," *ACS Nano* **5**, 2142–2146 (mar 2011).

[13] Huang, P. Y., Ruiz-Vargas, C. S., van der Zande, A. M., Whitney, W. S., Levendorf, M. P., Kevek, J. W., Garg, S., Alden, J. S., Hustedt, C. J., Zhu, Y., Park, J., McEuen, P. L., and Muller, D. A., "Grains and grain boundaries in single-layer graphene atomic patchwork quilts," *Nature* **469**, 389–392 (jan 2011).

[14] Demers, H., Poirier-Demers, N., Couture, A. R., Joly, D., Guilmain, M., De Jonge, N., and Drouin, D., "Three-dimensional electron microscopy simulation with the CASINO Monte Carlo software," *Scanning* **33**(3), 135–146 (2011).

[15] CRYTUR, "YAG:Ce Technical Parameters."

[16] Hass, G. and Waylonis, J. E., "Optical Constants and Reflectance and Transmittance of Evaporated Aluminum in the Visible and Ultraviolet," *Journal of the Optical Society of America* **51**, 719 (jul 1961).

[17] Instruments, T., "DLP7000 Technical Documents."

[18] Hamamatsu, "Photosensor module: H10721-210."

[19] Browne, M. and Ward, J., "Detectors for stem, and the measurement of their detective quantum efficiency," *Ultramicroscopy* **7**, 249–262 (jan 1982).

[20] Thorlabs, "PMT2101 - GaAsP Amplified PMT."

[21] Dyck, O., Kim, S., Kalinin, S. V., and Jesse, S., "Mitigating e-beam-induced hydrocarbon deposition on graphene for atomic-scale scanning transmission electron microscopy studies," *Journal of Vacuum Science & Technology B, Nanotechnology and Microelectronics: Materials, Processing, Measurement, and Phenomena* **36**, 011801 (jan 2018).

[22] Shevitski, B., Mecklenburg, M., Hubbard, W. A., White, E. R., Dawson, B., Lodge, M. S., Ishigami, M., and Regan, B. C., "Dark-field transmission electron microscopy and the Debye-Waller factor of graphene," *Physical Review B* **87**, 045417 (jan 2013).

[23] Guizar-Sicairos, M., Thurman, S. T., and Fienup, J. R., "Efficient subpixel image registration algorithms," *Optics Letters* **33**, 156 (jan 2008).

[24] Rudin, L. I., Osher, S., and Fatemi, E., "Nonlinear total variation based noise removal algorithms," *Physica D: Nonlinear Phenomena* **60**, 259–268 (nov 1992).

[25] Mardia, K. V. and Jupp, P. E., eds., [*Directional Statistics*], Wiley Series in Probability and Statistics, John Wiley & Sons, Inc., Hoboken, NJ, USA (jan 1999).

[26] Chen, Y. H., Park, S. U., Wei, D., Newstadt, G., Jackson, M. A., Simmons, J. P., De Graef, M., and Hero, A. O., "A Dictionary Approach to Electron Backscatter Diffraction Indexing," *Microscopy and Microanalysis* **21**, 739–752 (jun 2015).

[27] Brown, L., Hovden, R., Huang, P., Wojcik, M., Muller, D. A., and Park, J., "Twinning and Twisting of Tri- and Bilayer Graphene," *Nano Letters* **12**, 1609–1615 (mar 2012).